Data Mine

Documentation of Surface Fault Rupture and Ground-Deformation Features Produced by the 4 and 5 July 2019 M_w 6.4 and M_w 7.1 Ridgecrest Earthquake Sequence

Daniel J. Ponti*, *et al.*

Abstract

The M_w 6.4 and M_w 7.1 Ridgecrest earthquake sequence occurred on 4 and 5 July 2019 within the eastern California shear zone of southern California. Both events produced extensive surface faulting and ground deformation within Indian Wells Valley and Searles Valley. In the weeks following the earthquakes, more than six dozen scientists from government, academia, and the private sector carefully documented the surface faulting and ground-deformation features. As of December 2019, we have compiled a total of more than 6000 ground observations; approximately 1500 of these simply note the presence or absence of fault rupture or ground failure, but the remainder include detailed descriptions and other documentation, including tens of thousands of photographs. More than 1100 of these observations also include quantitative field measurements of displacement sense and magnitude. These field observations were supplemented by mapping of fault rupture and ground-deformation features directly in the field as well as by interpreting the location and extent of surface faulting and ground deformation from optical imagery and geodetic image products. We identified greater than 68 km of fault rupture produced by both earthquakes as well as numerous sites of ground deformation resulting from liquefaction or slope failure. These observations comprise a dataset that is fundamental to understanding the processes that controlled this earthquake sequence and for improving earthquake hazard estimates in the region. This article documents the types of data collected during postearthquake field investigations, the compilation effort, and the digital data products resulting from these efforts.

Cite this article asaa Ponti, D. J., J. L. Blair, C. M. Rosa, K. Thomas, A. J. Pickering, S. Akciz, S. Angster, J.-P. Avouac, J. Bachhuber, S. Bacon, *et al.* (2020). Documentation of Surface Fault Rupture and Ground-Deformation Features Produced by the 4 and 5 July 2019 M_w 6.4 and M_w 7.1 Ridgecrest Earthquake Sequence, *Seismol. Res. Lett.* **XX**, 2942–2959, doi: 10.1785/0220190322.

Introduction

The July 2019 Ridgecrest earthquake sequence included two large earthquakes that each produced extensive surface faulting and shaking-related ground deformation in Indian Wells Valley and Searles Valley, within the eastern California shear zone of southern California. Much of this deformation occurred within the boundary of the Naval Air Weapons Station China Lake (NAWSCL) where civilian access is restricted (Fig. 1). In the weeks following the earthquakes, surface faulting and ground deformation features were documented in the field by more than six dozen geologists and other scientists from the California Geological Survey (CGS), U.S. Geological Survey (USGS), National Aeronautics and Space Administration (NASA), U.S. Navy, and numerous universities and commercial firms. These researchers worked together in the field with the coordination and support of the California Earthquake Clearinghouse (Earthquake Engineering Research Institute [EERI], 2020) and the U.S. Navy, whose personnel were also instrumental in arranging access and for providing support for field activities within the boundary of the NAWSCL. To support emergency response efforts and planning for field investigations and instrument deployments, data collected in the field were rapidly synthesized by USGS and CGS office teams (Pickering *et al.*, 2019), and provisional maps of observation sites and fault rupture were updated on a regular basis and disseminated through the California Earthquake Clearinghouse,

Full author list and affiliations appear at the end of this article.

*Corresponding author: dponti@usgs.gov

the Earthquake Engineering Research Institute's Virtual Clearinghouse website (see Data and Resources) and the Southern California Earthquake Center's (SCEC) earthquake response blog (see Data and Resources).

Field documentation of earthquake effects, including the length and continuity of surface faulting, amount and sense of fault slip, and the occurrence and nature of shaking-induced ground failure, is fundamental to evaluating earthquake processes and for assessing earthquake hazards. In the case of the Ridgecrest earthquake sequence, postearthquake geologic activities included an initial reconnaissance phase during the first few days after the events, followed by a data collection phase that extended into December 2019. The initial reconnaissance phase focused on quickly determining overall fault-rupture location and extent, maximum coseismic fault slip, possible postseismic creep, and areas and extent of ground failure due to liquefaction and slope failure. This information provided critical situational awareness for emergency response and recovery efforts, for guiding seismic and geodetic instrument deployments, and for acquiring airborne light detection and ranging (lidar) and other imagery (Hudnut *et al.*, 2020) to support follow-on research. The data collection phase included detailed observations and mapping of faulting and ground-deformation features. Detailed field measurements of slip vectors derived from offset features or observed slickenlines on fault planes provide insight into rupture dynamics (e.g., Haddon *et al.*, 2019) and fault kinematics. Slip distributions along strike and data on rupture extent (Olson *et al.*, 2019; DuRoss *et al.*, 2020) offer important constraints for finite fault models, dynamic rupture simulations, and strong ground motion modeling (e.g., Hough *et al.*, 2019; Pollitz *et al.*, 2019; Thomas *et al.*, 2019; Lozos and Harris, 2020) and facilitate the comparison of field-based and remotely sensed observations (Gold *et al.*, 2019). Maps of fault rupture provide insights into cross-fault interactions (e.g., Hudnut *et al.*, 2019) and how faults may, or may not, be linked. Maps detailing rupture complexity and the association of coseismic rupture with existing tectonic geomorphology provide important insights into long-term fault activity and for refining fault hazard zones (e.g., Dawson *et al.*, 2019; Thompson Jobe *et al.*, 2019). Reconnaissance teams also identified and documented localized slip on both previously mapped and unmapped faults (Bilham and Costello, 2019; Hernandez and Dawson, 2019), further highlighting other potentially active fault zones within the region. In addition to surface faulting, both earthquakes produced shaking-related ground deformation associated with liquefaction and slope failure; these features were also documented in detail throughout the epicentral area.

Recent technological advances, such as data collection software that can run on smartphones and mobile tablets, allow for the simultaneous capture of notes, photographs, video and audio clips, and Global Positioning System (GPS) or Global Navigation Satellite Systems (GNSS) coordinate information. As a result, it is now possible to rather easily collect, compile, disseminate, and most importantly preserve large volumes of original field data in formats that can be readily accessed and searched. Similar to the postearthquake effort following the 2014 South Napa earthquake (Ponti *et al.*, 2019a,b), CGS and USGS collected and compiled field observations and data from all contributing researchers involved in the Ridgecrest postearthquake field-response effort. This article describes what data were captured following the earthquakes and how they were compiled. In a companion USGS data release (Ponti *et al.*, 2020), we present comprehensive documentation of observable faulting and surface deformation produced by the Ridgecrest earthquake sequence. These data include: (1) site-specific observations with field descriptions, displacement measurements, and photographs, and (2) maps of surface rupture that integrate the field observations with field-based mapping, airborne imagery, lidar, and satellite-based geodetic imaging products. We anticipate these datasets to be updated and added to incrementally as information is obtained, compiled and reviewed to produce an extensive curated collection of field observations and a comprehensive large-scale regional map showing all documented zones of surface faulting and ground deformation produced by the Ridgecrest earthquake sequence.

Data Collection

The first of two major earthquakes in the Ridgecrest sequence was an M_w 6.4 that occurred at 10:33 a.m. Pacific Daylight Time (PDT) on 4 July 2019 with an epicenter located approximately 17 km northeast of the town of Ridgecrest, California (Fig. 1). Early aftershock locations and initial media reports of damage to Highway 178 indicated a unilateral rupture to the southwest of the epicenter with left-lateral slip along a northeast–southwest-striking fault zone (Stewart *et al.*, 2019). By the evening of 4 July, field reconnaissance teams had arrived in the area and documented approximately 40–50 cm of left-lateral offset distributed across a 165 m wide zone crossing Highway 178. The following day, both ground and helicopter reconnaissance had identified most of the extent of northeast–southwest rupture. That evening, at 8:19 p.m. PDT, an M_w 7.1 earthquake nucleated at a depth of 8 km about 11.5 km northwest of the M_w 6.4 epicenter and ruptured bilaterally along a northwest–southeast-striking dextral fault zone. Fault rupture from this second event intersected the northeast portion of the M_w 6.4 rupture and, as documented later that night, ruptured Highway 178 approximately 5 km east of the M_w 6.4 offsets (Fig. 1). Field work to document both rupture zones and shaking-induced ground failure intensified over the next several weeks. Because access to the NAWSCL was generally limited to researchers from CGS and USGS, nongovernment researchers focused their efforts outside of the base, whereas USGS and CGS geologists mostly worked together within the NAWSCL boundary, accompanied by escorts and scientists from the U.S. Navy. Overall, more than six dozen researchers from 20

different government agencies, universities, and commercial firms contributed their observations to compilers at USGS and CGS, either directly or through the Clearinghouse.

In the days following the M_w 7.1 event, several kinds of products derived from satellite optical and radar images became available to field teams via the SCEC response blog (see Data and Resources), NASA's Advanced Rapid Imaging and Analysis data portal (see Data and Resources), the USGS Hazards Data Distribution System (see Data and Resources), and other online sources. These included (1) postearthquake commercial optical satellite imagery (WorldView 2, WorldView 3, Planet Labs, and Pleiades satellites); (2) Interferometric Synthetic Aperture Radar (InSAR) products from C-band Sentinel-1 and L-band Advanced Land Observation Satellite-2 satellites (e.g., interferograms, phase gradient, and line-of-site displacement maps); and (3) lineament maps derived from correlation analysis of pre- and postearthquake satellite imagery and radar products. These rapidly generated remote-sensing products were particularly useful for identification of potential faults or areas of ground failure far from the main fault ruptures. They helped verify continuity of rupture in areas that were inaccessible or where only discontinuous rupture could be seen in the field, and were also useful for quantifying fault slip in areas where deformation was distributed across broad zones and multiple fault strands, and thus difficult to evaluate in the field. Lineaments interpreted from these remote methods, however, do not preserve the details of deformation that can be observed on the ground. In addition, some lineaments may be confused with processing artifacts, features that are unrelated to tectonic deformation, or may be associated with small amounts of distributed deformation that is not visible on the ground. Therefore, as the primary fault zone locations and slip distributions became clearly defined, emphasis was given to field

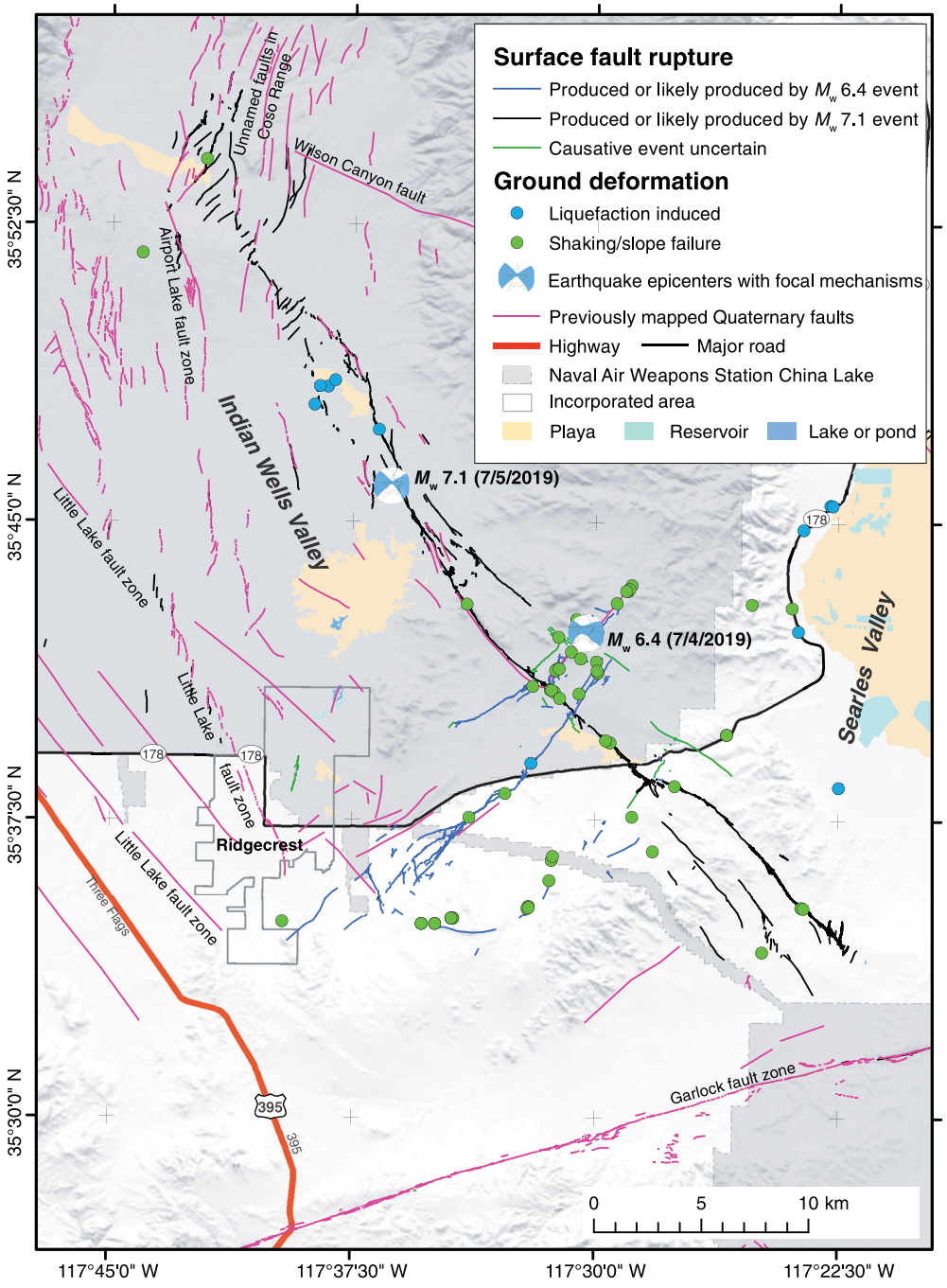

Figure 1. Map showing extent of surface faulting produced by the M_w 6.4 and M_w 7.1 Ridgecrest earthquake sequence, as verified from field observations as of December 2019 (black, blue, and green lines). Also shown are generalized locations of shaking-induced ground failure (circles), and traces of Quaternary-age faults that had been mapped at various scales (U.S. Geological Survey and California Geological Survey [USGS and CGS], 2006) prior to the 2019 earthquakes (magenta lines). Base from USGS – The National Map, 3D Elevation Program, and Hydrography Dataset, refreshed January 2020.

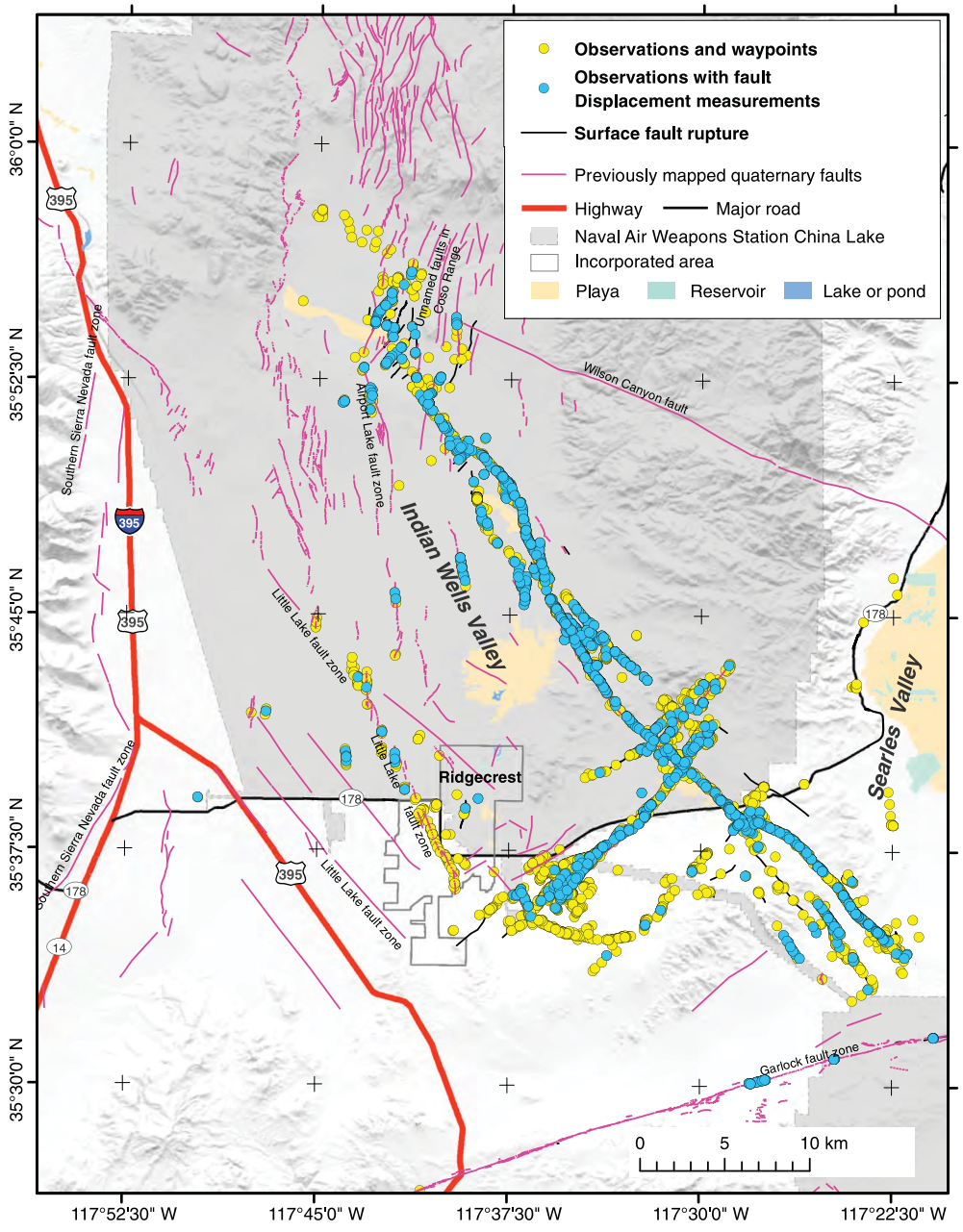

Figure 2. Map showing locations of ground-based field observations compiled as of December 2019. Yellow circles represent locations where notes or photographs were obtained (observations) or where the presence or absence of faulting was noted (waypoints). Blue circles are observations that include quantitative displacement measurements. Thin black lines represent surface rupture from the July 2019 earthquakes; magenta lines are previously mapped Quaternary-age faults (USGS and CGS, 2006). Base from USGS – The National Map, 3D Elevation Program, and Hydrography Dataset, refreshed January 2020.

verification of faulting and ground deformation inferred along lineaments identified from these remote-sensing products.

Through December 2019, we have collected more than 6000 site-specific ground observations (Fig. 2), approximately 6500 aircraft observations, and more than 25,000 photographs. Approximately 1500 ground observations noted only the presence or absence of faulting, but about 4500 also include descriptions, sketches, notes, and photographs, including more than 1100 observations that contain quantitative field measurements of horizontal and vertical components of fault slip and ground displacement (Figs. 3 and 4).

In addition to site-specific observations, field work also included mapping fault rupture and ground deformation along select portions of the primary rupture zones. These mapped features are represented by digital geological linework that was generated in several ways: (1) mapping directly in the field by walking along ruptures and recording tracks using both handheld and survey-grade GPS or GNSS receivers; (2) collecting waypoints along fault traces using handheld GPS or GNSS receivers and then producing linework by connecting the waypoints together using Geographic Information Systems (GIS) software; or (3) using GIS software to map directly onto high-resolution orthorectified aerial imagery and digital surface models obtained by small Unmanned Aerial Vehicles (UAVs) and processed using structure-from-motion applications (Donnellan *et al.*, 2019; Pierce *et al.*, 2020). Natural and man-made offset features were also surveyed using high-precision GNSS systems, including dirt road berms, tire tracks, stream channel margins, bedrock drainages, and other quasilinear features that could be used for computing fault offsets.

Data Compilation Procedures and Data Products

Site observations

Site observations of fault rupture and ground deformation were submitted directly from field participants to USGS and

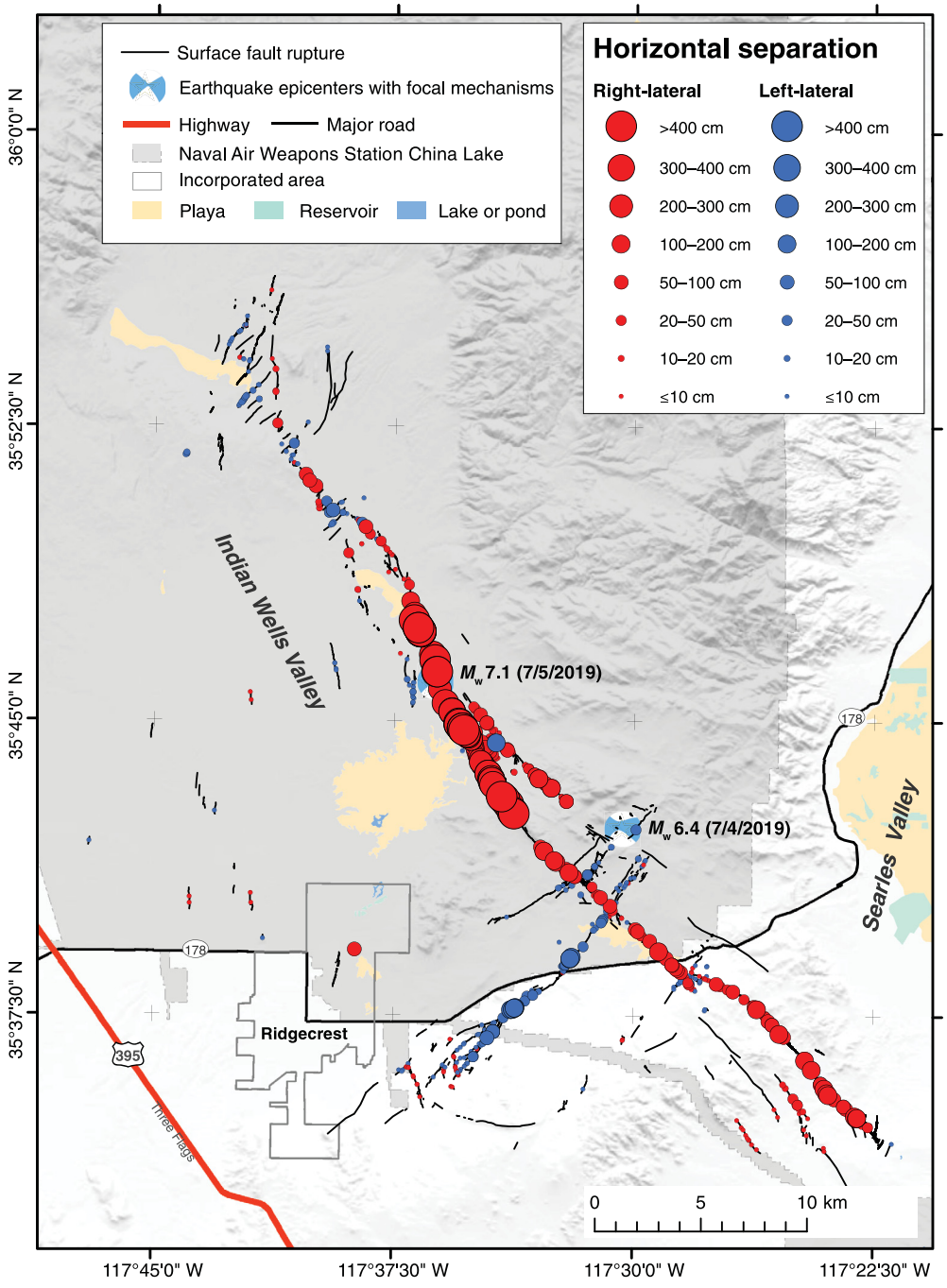

Figure 3. Map showing ground-based field observations obtained following the Ridgecrest earthquakes of July 2019, in which horizontal separation was measured. Red circles represent dextral slip and blue circles represent sinistral slip. Circle diameters represent amount of separation, in centimeters, as shown in legend. Base from USGS – The National Map, 3D Elevation Program, and Hydrography Dataset, refreshed January 2020.

CGS compilers or via the California Earthquake Clearinghouse. Observations included in our compilation consist of notes, descriptions, measurements, and photographs or sketches that document the existence and character of faulting or ground deformation at a geographic point. Observations of damage to buildings or earthen structures such as embankments or fills are documented elsewhere (Mosalam *et al.*, 2019; Stewart *et al.*, 2019; EERI, 2020) and are not included in our compilation unless they reflect permanent deformation of the natural ground surface.

Observations of fault rupture and ground deformation were documented at various levels of detail, which required standardization and reconciliation among different source datasets. Investigators used a variety of methods to record site observations in the field and reported information in a number of digital formats, such as spreadsheet tables, GPS or GNSS track logs, reports as pdf files, photographs or scanned drawings in several image file formats, text documents (email, text, or word processing files), ESRI shapefiles and geodatabases, and Keyhole markup language (kml or kmz) files. In addition to the different data formats, the recorded information was organized or classified in different ways depending on the observers' standards of practice. Site-specific data we received fall into one or more of these categories:

1. *Waypoints*. Point data attributed only with the presence or absence of faulting or ground deformation.
2. *GPS or GNSS track logs*. Points along ground traverses or flight lines, showing where investigators had traveled during reconnaissance. Track logs were used for identifying data gaps during field work and for geocoding time-based observations and photographs, but raw track log data are not included in the compilation.
3. *Descriptions and notes*. Descriptions of fault rupture or ground deformation referenced to a location or notes about the observation.

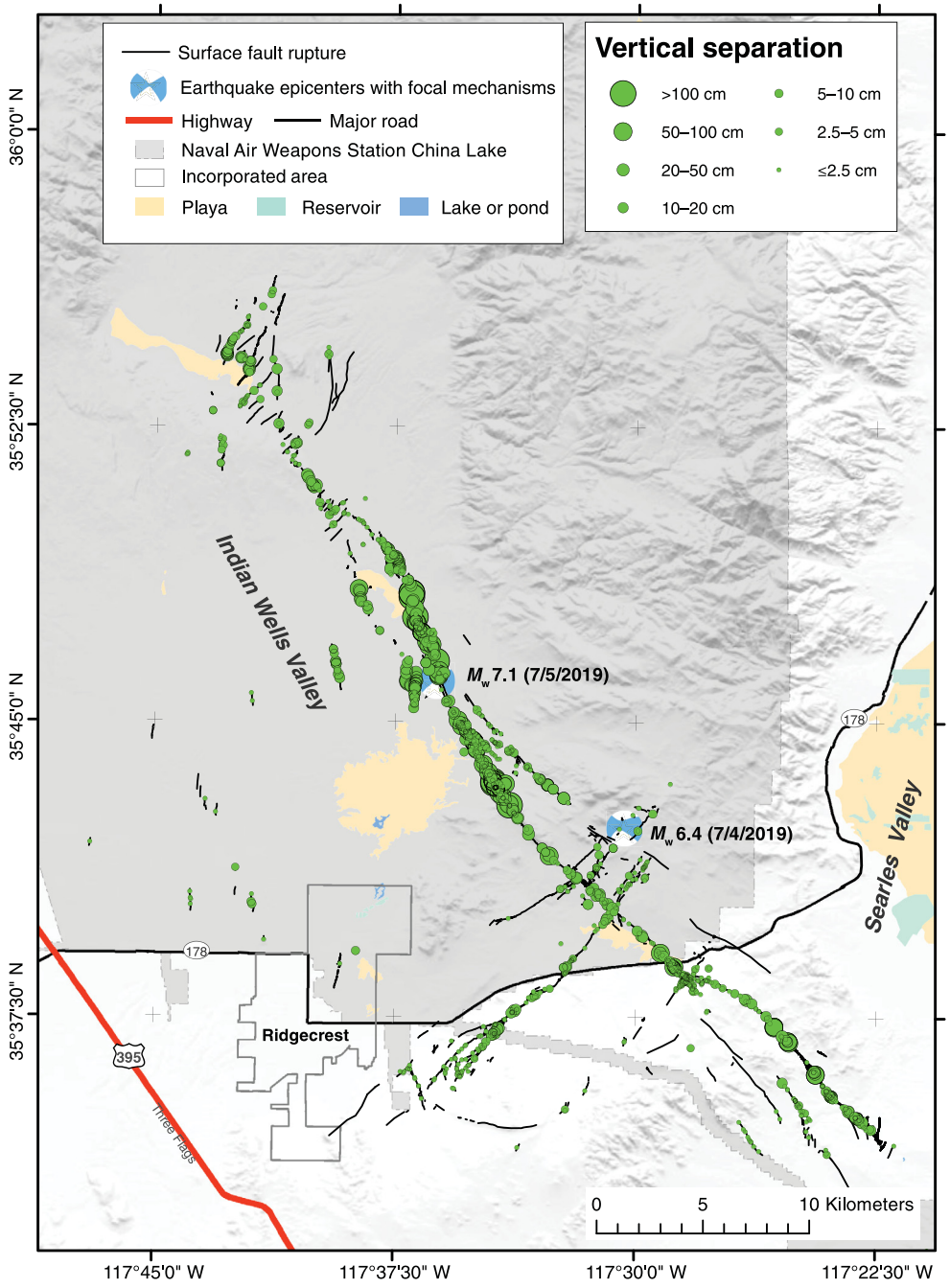

Figure 4. Map showing ground-based field observations obtained following the Ridgecrest earthquakes of July 2019, in which vertical separation was measured (green circles). Circle diameters represent amount of separation, in centimeters, as shown in the legend. Base from USGS – The National Map, 3D Elevation Program, and Hydrography Dataset, refreshed January 2020.

4. *Digital photographs or sketches*. Photographs or drawings of fault rupture or ground deformation features, with or without embedded coordinate information or other camera metadata. Only internally geocoded photos or photos that are explicitly referenced to a locality are included in the compilation. Duplicate, out-of-focus, or extraneous photos were omitted. All photos taken within the NAWSCL boundary required screening by U.S. Navy personnel before they could be made public, and any photos that did not meet security requirements were also omitted from the compilation.
5. *Measurements*. Quantitative fault separation and fracture offset data compiled into a spreadsheet or other type of table or recorded in a text description.

Observation compilation procedures. Apart from GPS or GNSS track logs, all contributed site data were extracted from their original formats, parsed, and loaded into a spatial database using a compilation schema developed by USGS and CGS that consists of two primary tables: (1) an observation table that holds notes, descriptions, location information, and displacement measurements and (2) a photo table for associated photos and sketches, including photo Exchangeable Image File Format (Exif) and GPS metadata, with links to the associated digital image files. There is a one-to-many relationship between observation records and photo records such that each photo record is associated with a single observation record via an internal identifier that is assigned during compilation. Each record in the observation table represents an observation of faulting, ground deformation, or no deformation that was made by an investigator or field team working together (an observer) during a unique visit on a specific date. If the same observer or team revisits the same locality on a different day or time and records

TABLE 1
Summary of Information Stored in the Observation Data Table

Data Category	Category Definition	Attributes
Observation record metadata	Information required for all observation records	Internal identifier, observer identifier (if given); observation date and time (local time zone); principal observer; observer affiliation; field team identifier; observer position (at site, aircraft, etc.); site location as reported (latitude and longitude); observation type (e.g., tectonic, liquefaction, shaking, no deformation, etc.), and citation (if also published elsewhere)
Rupture or deformation characteristics	Qualitative information about fault or fracture geometry, orientation, and surface expression	Notes and descriptions; fault expression; fault azimuth with uncertainty; fault dip with uncertainty; local fracture azimuth with uncertainty; rupture width with uncertainty; presence of fault gouge; visible striations; and scarp-facing direction
Displacement measurements	Quantitative information about displacement magnitude and sense of motion	Observed offset feature; slip-vector length, azimuth and plunge with uncertainty; horizontal separation azimuth with uncertainty; horizontal separation with uncertainty; vertical separation with uncertainty; extensional or compressional separation with uncertainty; measurement aperture with uncertainty; and displacement sense
Compilation fields	Information entered during compilation, as applicable	Adjusted location, strike-slip displacement, dip-slip displacement, compiler notes, and inferred earthquake source event

Full documentation of table attributes is provided in the data repository (Ponti *et al.*, 2020).

a separate observation, this constitutes a separate record in the observation table. Similarly, observations made by different field teams at the same locality are preserved as separate observation records. The types of information stored within the observation and photo tables are summarized in Tables 1 and 2, respectively. Full documentation of the observation and photo table attributes are given in Federal Geographic Data Committee (FGDC) metadata files that accompany the data products themselves (Ponti *et al.*, 2020). The goal of the compilation is to present the data as reported, interpreted only as necessary to assemble the information into the compilation schema and with as much metadata about the observation as possible. We apply no measure of field quality; future researchers can evaluate the reported data for their purposes by assessing measurement completeness, reported uncertainties and measurement approaches, variability of multiple measurements at the same site or nearby, and by evaluation of photographic evidence.

A principal challenge for data compilation was the extraction, parsing, and translation of observations from multiple data sources into the compilation schema. To simplify this process, several investigators contributed observations using a spreadsheet template designed to mimic the compilation schema. In addition, many CGS and USGS investigators collected field data with ESRI's ArcCollector application, using a data entry schema initially developed by CGS, but that was modified several times during data collection to better fit with field conditions and the compilation database schema. ArcCollector interfaces with ArcGIS Online and by synchronizing to master maps, data collected are made available to compilers and field investigators in as close to real time as possible. Although this application greatly assisted in providing situational awareness to investigators and compilers, and simplified data compilation, significant amounts of manual parsing, and extraction of ArcCollector data were still necessary.

When parsing reported data into the compilation database, care was taken to preserve as much of the originally reported information as possible. All notes recorded by observers were preserved exactly as written, except in the following cases: (1) typographical or grammatical errors were corrected, acronyms expanded, and jargon omitted or translated; (2) references to other observation sites were changed, if necessary, to the compilation ID, to ensure that the appropriate sites are referenced; and (3) personally identifiable data and irrelevant information were removed.

Observation location uncertainties. Most observations were recorded using mobile applications running on smartphones, mobile tablets, or satellite-navigation-enabled cameras, and reported location coordinates were obtained from the GPS or GNSS chipsets included with these devices. The remaining observation locations were generally recorded using handheld or high-precision GNSS devices. For some observations, the specific satellite-navigation device was reported or could be inferred (e.g., observations recorded using CGS' ArcCollector application all used Apple iPad tablets for input),

TABLE 2
Summary of Information Stored in the Photo Data Table

Data Category	Category Definition	Fields
Photo record metadata	Information required for all photo records	Identifier; observation id (foreign key); photographer, photo file name; creation date and time (local time zone); image size; file Uniform Resource Locator (URL); observation location (latitude and longitude); photo location (latitude and longitude); and photo caption (if available)
Exif data	Camera settings	F-stop; shutter speed; focal length; hyperfocal distance; field of view; camera model; lens information; light value; metering mode; white balance; and digital zoom ratio
Global Positioning System (GPS) data	For image files with embedded GPS info	GPS latitude; GPS longitude; GPS altitude; GPS image direction; GPS image direction reference (e.g., magnetic or true north); and GPS satellites
Compilation fields	Information entered during compilation as applicable	Adjusted location (if required) and compiler notes

Full documentation of table attributes is provided in the data repository (Ponti *et al.*, 2020).

but in many cases the specific satellite-navigation device was not reported. Published studies comparing the horizontal accuracy of cell phones to stand-alone GNSS devices indicate that newer phones with assisted GPS or GNSS can achieve similar accuracies and acquire a positional lock faster than stand-alone devices (Jones *et al.*, 2015). Horizontal accuracy can vary widely, however, from less than 2.5 m for stand-alone devices, and from less than 10 to more than 200 m for cell phones and tablets, depending on model, network provider, satellite geometry, and local conditions (Jones *et al.*, 2015).

We infer that the accuracy of most all reported locations is on the order of 10 m or less, comparable to those reported previously, based on comparison of different observations at collocated sites, or when comparing against known locations on high-resolution orthoimagery. In a few cases, discrepancies of more than several hundred meters were noted. The largest errors appear to be associated with observations that were recorded before the satellite receiver acquired a positional lock. By default, phone- and tablet-navigation software applications usually do not provide much information to the user about how the satellite receiver is functioning, nor is that information typically reported as part of the observation.

As discussed in the following, site-observation data are initially published as provisional releases. Provisional data releases use the originally reported location coordinates; no adjustments are made, except for cases in which significant errors in the originally reported coordinates were noted and the correct location can be recovered. Finalized datasets include the location coordinates as originally reported and also record "final" locations that result from reconciling the observation locations against maps of fault rupture. If necessary, the site-location coordinates are adjusted to place the observations in their correct location relative to the associated rupture feature.

Slip and separation measurements. The M_w 6.4 fault rupture is dominated by northeast–southwest-striking fault traces that exhibit left-lateral horizontal separation, whereas the M_w 7.1 fault rupture is dominated by northwest–southeast traces that exhibit right-lateral separation. Both rupture zones are highly complex, with faulting expressed as zones of vertical scarps, en echelon fractures, surface cracks, mole tracks, and orthogonal, conjugate cross faults (Kendrick *et al.*, 2019). Locally, zones of deformation extend hundreds of meters from the main rupture. Significant vertical offsets also occur locally as a result of normal or reverse components reflective of extension or compression at some angle to the general fault strike.

Along any given rupture trace, all components of fault slip and displacement sense can be derived by measuring fault strike (fault azimuth) and the length, plunge, and azimuth of the slip vector, which is a line that connects a point on a feature (piercing point) with the equivalent point on the feature after it has been cut and moved apart by fault displacement (see Fig. 5). In many cases, it is difficult to measure slip-vector attributes directly, but the strike-slip displacement component can be derived if the fault azimuth is measured and (1) if the horizontal length and azimuth of the line that separates the piercing point can be measured (D_h in Fig. 5), or (2) if the horizontal separation of an offset feature and its azimuth (S_h and β_s in Fig. 5) are measured, provided there is no extension or compression or the offset feature is oriented perpendicular to the fault strike. The latter approach was used commonly for these earthquakes, given that the complexity of the rupture often made identification of precise piercing points difficult.

Observers typically report slip or separation amounts as a single value with no stated uncertainty, as a reported value plus or minus some uncertainty value or values, as a range of values, as an estimate, or as a minimum or maximum value. Reported

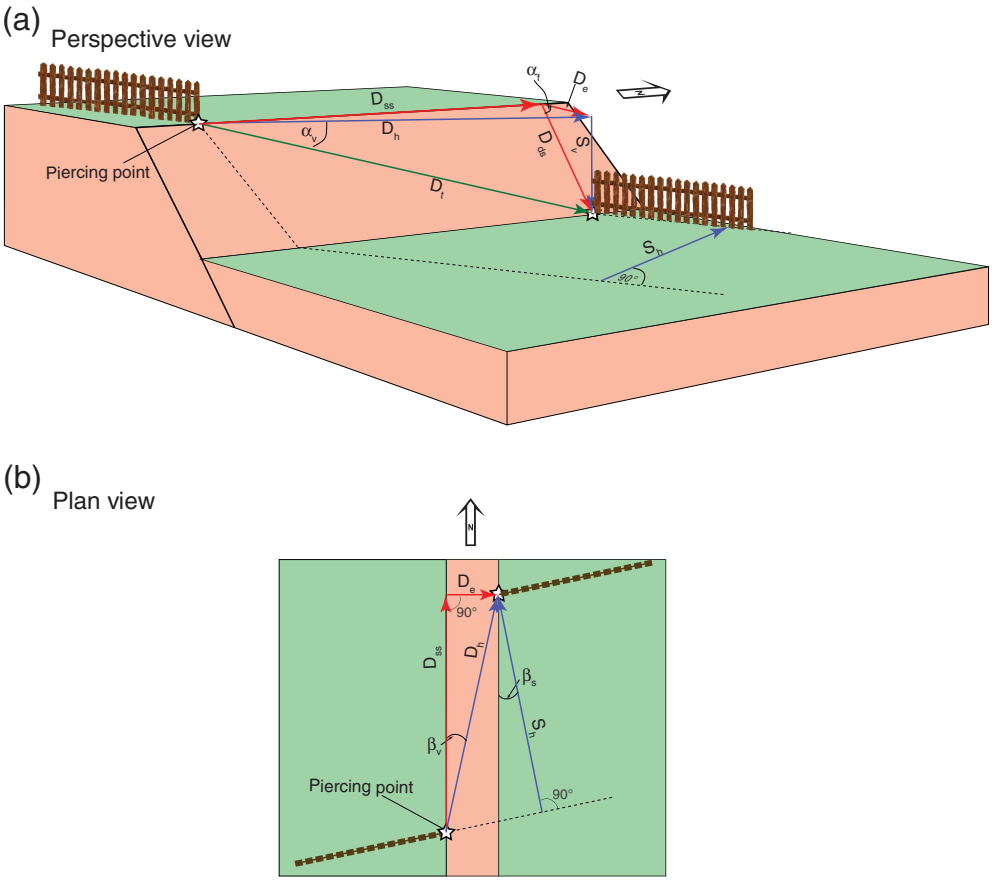

Figure 5. (a) Perspective view and (b) plan view diagrams illustrating left-normal offset of a fence across a north-striking fault and the various components of fault slip. Total slip on the fault (D_t) is defined by the slip vector (green) that lies on the fault plane and connects the piercing points (stars). Strike-slip (D_{ss}), dip-slip (D_{ds}), extensional (or compressional) slip (heave, D_e), (red) and fault dip (α_f) can be derived by measuring the vector length (D_t), plunge (α_v), and the angle between the fault-strike and slip-vector azimuth (β_v). Measuring the slip vector directly in the field, however, is often difficult, so what is commonly reported is either the horizontal component of the slip vector (D_h) or horizontal separation of an offset feature (S_h), measured normal to the feature azimuth, and the vertical separation (S_v), shown in blue. If measurement azimuths and fault strike are recorded, then $D_{ss} = D_h \cos(\beta_v)$. If horizontal separation is recorded, $D_{ss} = S_h / \cos(\beta_s)$ provided the fault dip is vertical, there is no extension or compression, or the azimuth of the offset feature is oriented normal to the fault strike. Most all of the measured faults involved in the Ridgecrest earthquake sequence are steeply dipping, and therefore $S_h / \cos(\beta_s)$ is a good approximation for D_{ss}, and S_v also approximates D_{ds} in most instances. If there is significant fault heave and only horizontal separation (S_h) is measured, then vertical separation (S_v) and heave (D_e) must be measured independently if strike-slip and dip-slip displacements are to be accurately determined.

uncertainties are rarely, if ever, defined by the observers and are inferred to incorporate the full range of possible slip values at a site as opposed to some measurement of a particular probability distribution. As such, the observation table records slip or separation in preferred, minimum, and maximum value fields. For example, a reported slip or separation value of 20 ± 5 cm would have minimum, preferred, and maximum values recorded as 15, 20, and 25 cm, respectively, whereas slip or separation reported as a range (e.g., 20–50 cm) would record minimum (20 cm) and maximum (50 cm) values, but no preferred value. Similarly, slip or separation amounts reported as <20 cm or >5 cm, for example, would be recorded as maximum or minimum values only. Slip or separation amounts that are reported as estimates, as opposed to directly measured, are noted as such within the description or compilation notes fields in the observation record.

Only reported slip-vector attributes and horizontal, vertical, and fault-normal (heave) separation components, including recorded uncertainties, are reported for observations published in provisional form. Observations with slip or separation measurements published in final form also include computed values for strike-slip, dip-slip, and total slip amounts, provided that enough offset components were measured in the field to allow for the calculation. Where a horizontal separation and separation azimuth are measured but the fault azimuth is not recorded, the fault azimuth can be estimated from rupture maps to compute strike-slip displacement. Strike-slip displacements computed from estimates of fault azimuth are flagged in the observation table.

Two important measurements captured in the observation table, if reported, are values for rupture width (width of the fault zone measured normal to fault strike) and measurement aperture (the distance normal to fault strike, over which the slip measurement is taken). Most field measurements of fault slip are short aperture measurements using measurement tapes and hand compasses. Therefore, where faulting is distributed across a zone that is tens of meters across, reported measurements of short aperture likely underestimate total fault slip. Recorded values of rupture width and measurement aperture provide a qualitative means for evaluating how well a recorded slip value may represent total slip across the fault zone.

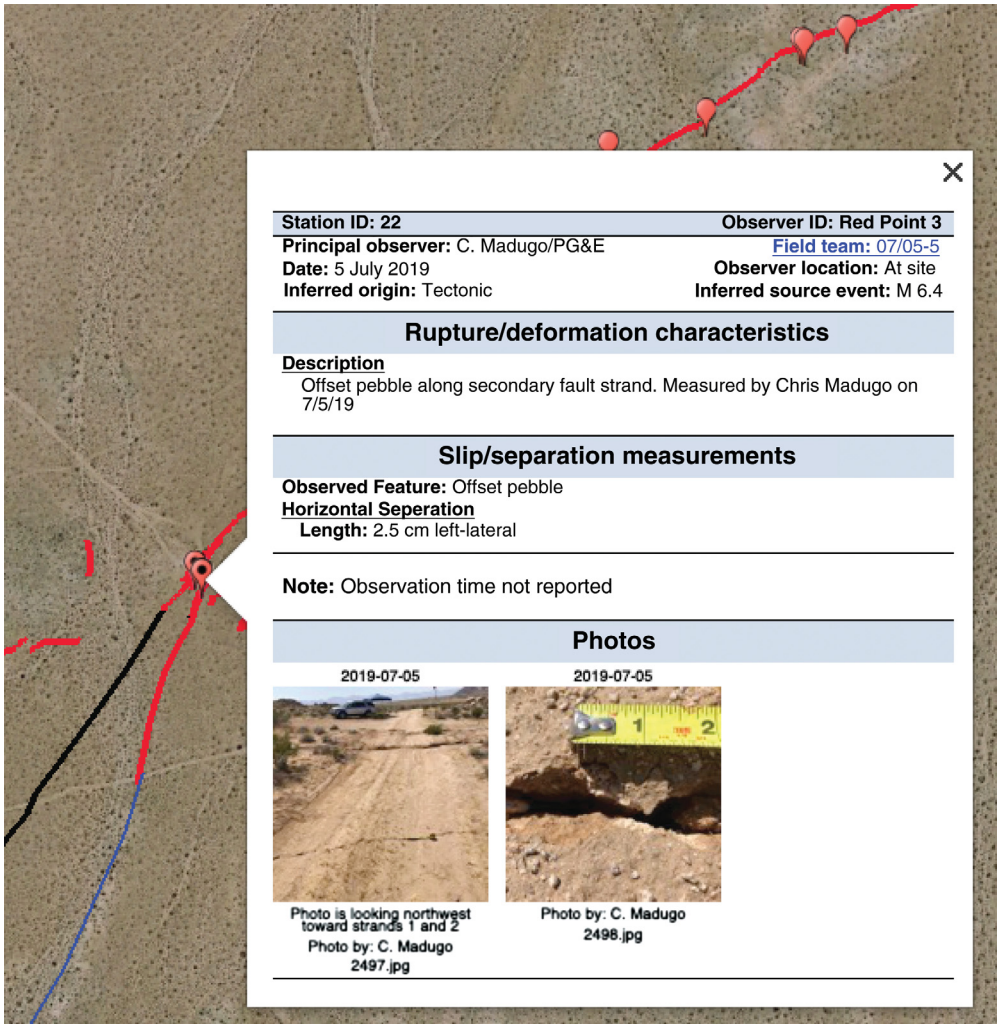

Figure 6. Example of one of the site-observation kmz data products overlain onto the provisional rupture map as displayed in Google Earth. Observation sites are shown as placemark symbols; clicking on the placemark symbol reveals a pop-up window with summary observation data and thumbnails of associated photographs. Clicking on a photo thumbnail will cause the full-resolution photo to be downloaded for viewing.

Site-observation data products. Site-observation data products are planned for release in stages as data are fully compiled, reviewed, and finalized. We plan to post all data products within a single online USGS data release (Ponti *et al.*, 2020). Anticipated product releases are as follows:

1. Provisional release of observation sites (including slip or separation measurements, notes, and descriptions) in which quantitative fault slip or separation data were collected (e.g., sites displayed in Figs. 3 and 4).
2. Provisional release of updated observations with quantitative displacement measurements, and associated photographs.
3. Provisional release of observation sites with qualitative data (e.g., notes or photos), including observations of slope failure and liquefaction as well as faulting.
4. Provisional release of waypoint observations (denotes only presence or absence of deformation).

Finalized versions of these datasets will include locations adjusted and fault-slip parameters computed, as discussed previously.

Each data product is planned to consist of the following data items, where applicable:

1. The observation table, in comma-separated variable (CSV) format, for input into spreadsheets, databases, and GIS applications.
2. The photo table, in CSV format, for input into spreadsheets, databases, and GIS applications.
3. Summary observation data and photo thumbnails, where present, provided in kmz format for viewing in Google Earth or similar applications. Each observation site is shown as a placemark; clicking on a placemark provides a pop-up window with summary site information and thumbnails of photographs associated with the observation (Fig. 6). Clicking on one of the photo thumbnails will display the full resolution photo on the user's computer.
4. Full-resolution digital photographs and sketches, where present, in Joint Photographic Experts Group (JPEG) format. These files can be downloaded from the data release website directly, or accessed via a URL in the photo table CSV file, or from the kmz product. Camera Exif and GPS metadata from the original photograph, plus other information assembled during compilation, such as photographer name and affiliation, data release DOI, copyright information, and photo caption, are embedded within each JPEG file.

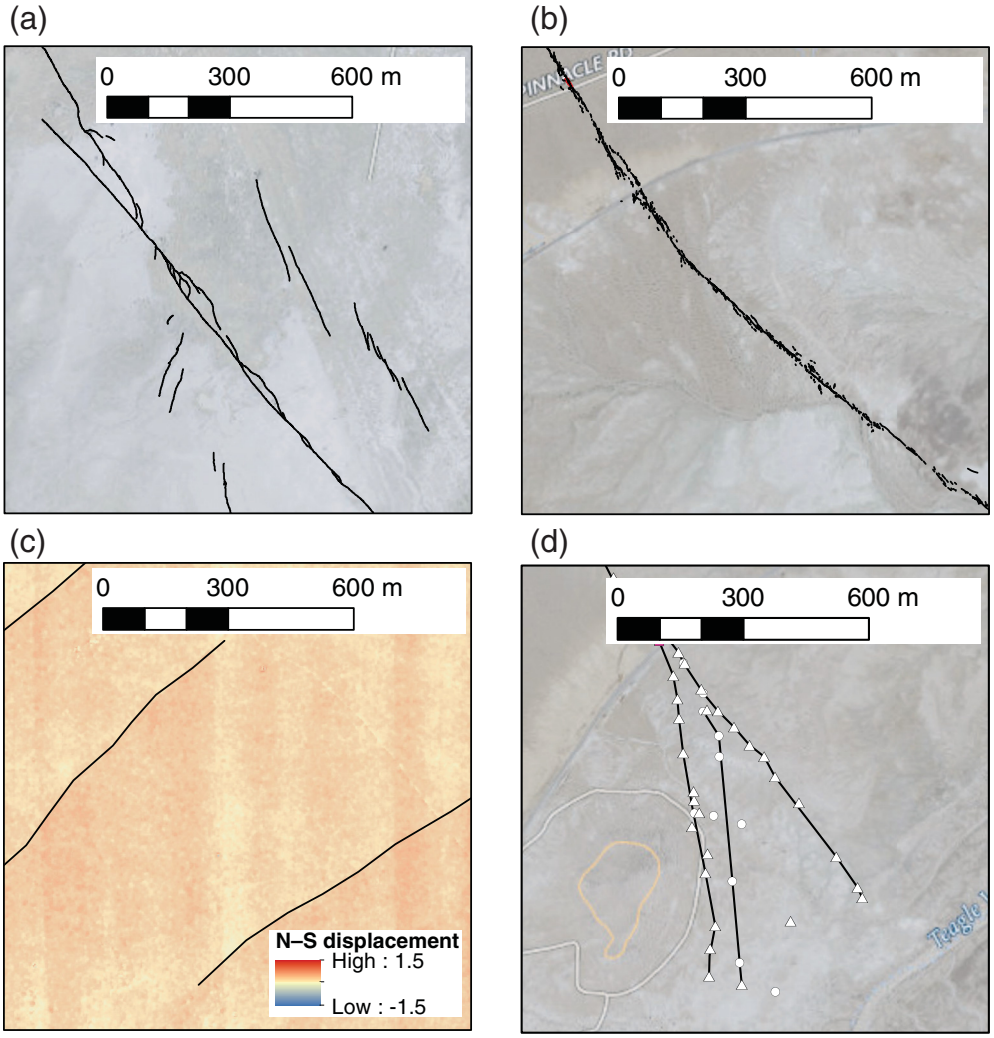

Figure 7. Representative examples of fault rupture linework by linework classification. See Provisional rupture and ground deformation maps section for explanation of the classifications. (a) Classification: Field; example is from the high-slip area of the M_w 7.1 rupture and shows linework produced by walking along ruptures using survey-grade Global Navigation Satellite Systems (GNSS) instrumentation. Linework by Scott Bennett. (b) Classification: Imagery; example shows linework near the southern end of the M_w 7.1 rupture derived from high-resolution drone orthoimagery, with ground-sample distance from 2 to 10 cm (Pierce *et al.*, 2020). Linework by Ian Pierce. (c) Classification: Remote sensing; example shows interpreted fault traces near the northern end of the M_w 7.1 rupture traced from optical pixel correlation imagery at 1:5000 compilation scale. Linework by Alex Morelan. (d) Classification: Inferred; example shows secondary fault traces located near the southern terminus of the M_w 7.1 rupture inferred to pass through or near rupture observation locations while maintaining smooth strike transitions. Points not on the inferred traces are either non-fault-related observations or reflect inherent variability in recorded locations. Circles are observation locations by Chris Milliner and Robert Zinke. Triangles are observation locations by Sinan Acziz, Selena Padilla, Alexandra Hatem, and James Dolan. Linework by Daniel Ponti. Base imagery as follows: (a), (b), and (d). USGS – The National Map, USGS Imagery Topo Basemap, refreshed January 2020; c) optical pixel correlation image showing north–south component of motion (color bar shows scale in cm), derived from WorldView 2 and WorldView 3 satellite images dated 23 June 2018 and 13 July 2019, respectively. Image produced by Alex Morelan using co-registration of optically sensed images and correlation (COSI-Corr) software (Leprince *et al.*, 2007).

Full documentation is provided in FGDC metadata files for each data item.

Rupture and ground deformation maps

In addition to documenting fault characteristics and displacement data at specific sites, a primary goal of this data compilation is to produce comprehensive maps of fault rupture and ground deformation features that were produced by the Ridgecrest earthquake sequence. As mentioned previously, portions of fault rupture and deformation features were mapped directly in the field, but most features were not completely documented on the ground. Development of comprehensive rupture and ground-deformation maps, therefore, requires that we integrate the field-based maps with observations and rupture interpretations derived from postearthquake airborne imagery, lidar, and geodetic imagery products.

Data from many sources were used to construct rupture maps. These include fault rupture and ground deformation linework provided directly to us from field teams, and linework compiled by (1) inferring the occurrence and strike of rupture from site observations and waypoints; (2) identifying mappable evidence of rupture on postearthquake optical imagery from satellite, aircraft, and UAV platforms; (3) interpreting the presence of rupture from lineaments observed on shaded relief images derived from postearthquake digital surface models; and (4) interpreting the presence of rupture from geodetic imaging products (InSAR and optical pixel correlation images). These different approaches each

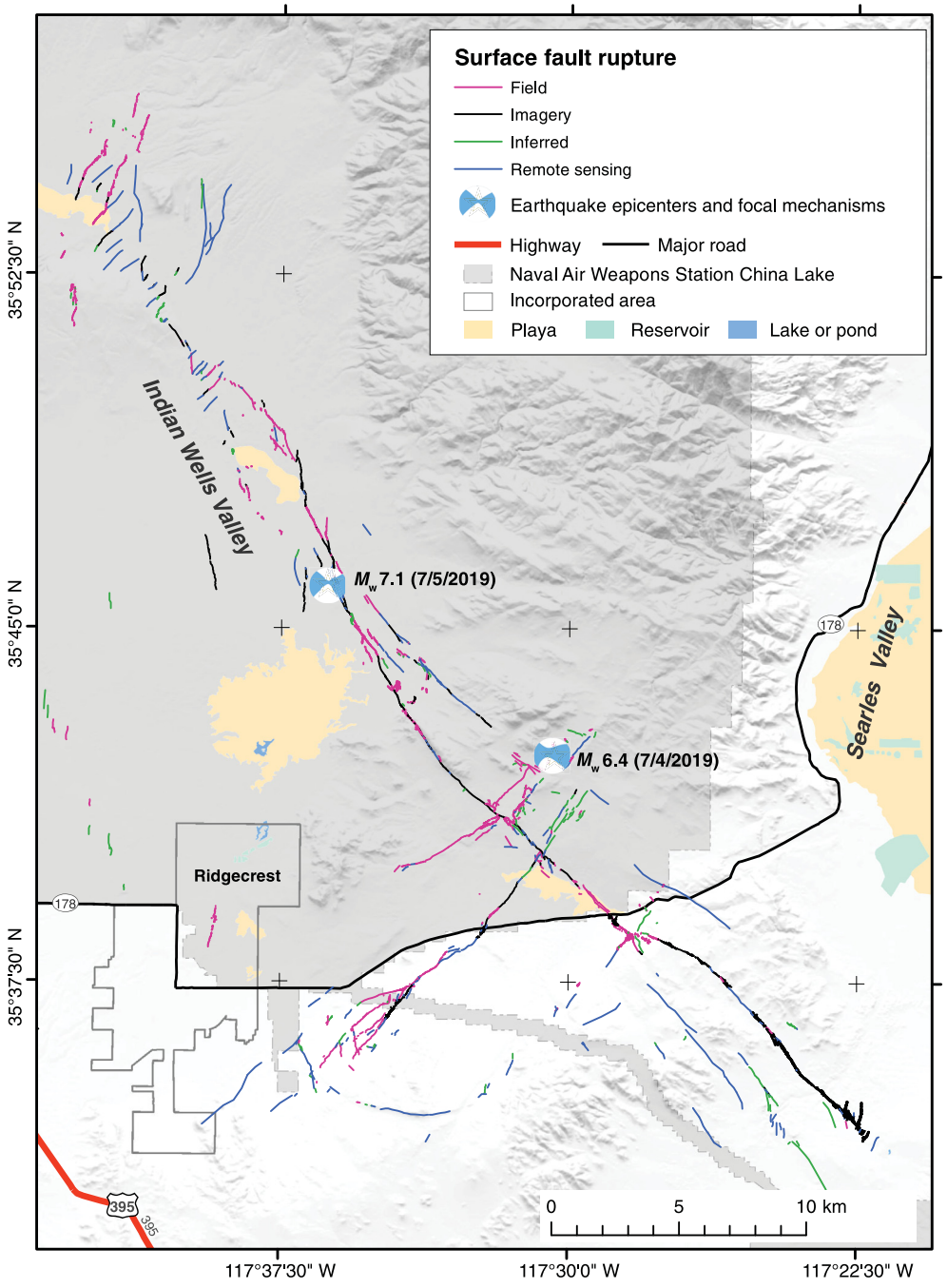

Figure 8. Provisional rupture linework showing extent of surface faulting produced by the M_w 6.4 and 7.1 Ridgecrest earthquake sequence, as verified from field observations as of December 2019. Rupture is symbolized by linework classification (see Provisional rupture and ground deformation maps section for explanation of the classifications). Base from USGS – The National Map, 3D Elevation Program, and Hydrography Dataset, refreshed January 2020.

represent fault rupture and ground deformation features at notably different levels of detail and location precision (Fig. 7).

Location uncertainties for rupture and ground deformation linework. Location accuracy reported for contributed linework created by use of survey-grade GNSS instruments is on the order of 3–20 cm horizontal and 5–30 cm vertical after postprocessing using four to five local permanent geodetic base stations (Bennett *et al.*, 2019; Scharer *et al.*, 2019). Linework derived from track logs and waypoints obtained from smartphone, tablet, or handheld satellite navigation receivers typically have location accuracies on the order of 2.5–10 m (Ponti *et al.*, 2019a) and tend not to preserve fine-scale detail of the rupture.

Linework produced from orthoimagery or geodetic imaging products is generated manually by visual inspection of the imagery at varying compilation scales, with location precision dependent on resolution of the imagery and location accuracy dependent on the control used for the base imagery; accuracy uncertainties can be as large as 10–20 m for some UAV datasets due to poor ground control. Resolution of UAV orthoimagery ranges between 1.53 and 10 cm ground sample distance, allowing for the ability to map fine-scale and small-displacement fractures. Resolution of satellite imagery and geodetic imaging products range from 0.3 to several meters depending on the specific dataset. Fine-scale rupture detail is typically not observable in these lower resolution or derivative products.

Provisional rupture and ground deformation maps. Provisional maps of fault rupture and ground deformation (Fig. 8) are composed of a "mashup" of linework from the various sources noted previously. If more than one linework representation exists for a segment of the fault rupture, linework showing the most rupture detail or best location accuracy, based on the judgment of the compiler, is preserved. In general, line segments from

detailed field-based maps or very high-resolution optical imagery or digital surface models are included in the provisional maps rather than lines derived from lower resolution satellite images, geodetic products, or fault-rupture traces inferred from observation sites or waypoints. On provisional maps, less than 25% of the linework is derived from high-resolution optical imagery and detailed field mapping. Because line segments from the various sources vary in location accuracy and precision based on the source equipment or imagery, mismatches can occur at the boundaries between linework from different sources. No corrections are made for these mismatches in the provisional maps.

Rupture maps are compiled using GIS software, and each line segment is attributed as follows:

1. *Classification*: an enumerated value that identifies the primary source for the rupture linework. Values are:
   a. *Field*: linework produced by direct mapping in the field.
   b. *Imagery*: linework produced by visual identification of rupture from postearthquake georeferenced orthoimagery or from imagery- or lidar-derived digital surface models. Linework detail is dependent on the compilation scale and resolution of the base imagery.
   c. *Remote sensing*: linework derived from pre- and postearthquake satellite-based radar and optical imagery using radar interferometry or optical image correlation methodologies. Useful in areas where displacements are too small to be visible in optical images. Fine-scale rupture details are not represented.
   d. *Inferred*: linework produced during compilation phase by inferring occurrence and strike of rupture from observations and waypoints; used in areas where deformation is known from ground observations but where no mapping was done in the field and where deformation is not visible on imagery or remote-sensing products; shows strike of faulting only; does not preserve rupture continuity; and may not include entire length of rupture along strike.
2. *Subclass*: an attribute that provides additional documentation to the classification value. For field, this attribute describes the field mapping technique (e.g., GPS or GNSS track, waypoint connection, etc.). For imagery and remote sensing, this attribute identifies the specific image file, image resolution, and compilation scale (if reported) for the interpreted linework.
3. *Verification*: an enumerated value that provides a qualitative evaluation of how well the line segment represents the extent and overall strike of the fault rupture or deformation feature in the field. Values are:
   a. *Yes*: rupture was directly mapped in the field, is clearly visible in postearthquake optical imagery, or is inferred where multiple observations of fault rupture or deformation occur along the strike of a feature such that its continuity and extent as mapped are well constrained.
   b. *Partial*: one or several site observations exist on the strike of the feature, but there is low confidence as to the overall extent and continuity of the rupture segment or where, based on observations, the fault rupture occurs over broad areas.
   c. *No*: line segments inferred from digital surface models or derivative remote-sensing products that have not been field checked. Used in working maps only; products for public release do not contain unverified linework.
4. *Provider*: name and affiliation of the field mapper or compiler who produced the linework.
5. *Date*: the date the rupture was mapped in the field, or if from imagery the date the image was acquired. For remote-sensing products that use image pairs, this is the date of the most recent (postearthquake) image used. Inferred line segments do not have a date assigned.
6. *Origin*: an enumerated value describing the inferred cause of the mapped feature, based on ground observations and other factors such as rupture continuity and surface expression. Values are:
   a. *Tectonic*: zone of deformation having strike and displacements consistent with the earthquake source mechanism and general surface rupture patterns. Sense of offset may be observed directly or inferred from patterns of en echelon surface fractures. Tectonic surface rupture includes both seismogenic rupture that has propagated to the surface from the earthquake source, and slip resulting from shallow strain release triggered by shaking or changes in near-surface stresses from the earthquakes.
   b. *Shaking*: inferred to have been produced solely by shaking-induced shallow slope failures and lateral spreads. Linear fractures represent head scarps of lateral spreads and landslides; closed lines bound regions of small-scale slumps, settlements, rockfalls, and bank failures.
   c. *Uncertain*: linear rupture segments in which the feature strike and displacement could be attributable to either faulting or lateral spreading. This value is also used for rupture segments in which the orientation and displacements measured in the field appear not to be consistent with the earthquake source mechanisms nor can the feature be readily attributable to typical earthquake induced ground-failure mechanisms, such as liquefaction or shallow slope failure.
7. *Source*: an enumerated value that identifies the inferred earthquake source that produced the mapped rupture, based on location, displacement sense, and field observations. Ruptures symbolized by this attribute are shown in Figure 1. Values are:
   a. M_w 6.4: rupture likely produced by the 4 July 2019 M_w 6.4 earthquake.
   b. M_w 7.1: rupture likely produced by the 5 July 2019 M_w 7.1 earthquake.

c. *Uncertain*: ruptures that are not readily attributable to either of the M_w 6.4 or 7.1 events (Fig. 1). These tend to be small displacement northeast–southwest-striking zones of fractures located some distance from, but approximately parallel to, the main M_w 6.4 rupture zone.

8. *Provider note*: any notes or descriptions submitted by the data provider.
9. *Citation*: if linework is published elsewhere, the author(s), date, and DOI of the publication.

Final rupture and ground-deformation map. A finalized map will require analysis of additional high-resolution imagery of the rupture area. Between 27 July and 2 August 2019, the National Center for Airborne Laser Mapping (NCALM) acquired airborne imagery over the epicentral area with a Titan multispectral lidar and imagery sensor, and USGS acquired GNSS ground-control data (Hudnut *et al.*, 2020). The lidar acquisition covered approximately 660 km^2 at 25 points/m^2, with an embedded 80 km^2 ultrahigh-resolution survey at 80 points/m^2 over the primary rupture zones. For the associated optical imagery, the digital pixel resolution is expected to be 4–6 cm. Point cloud data and a derivative digital surface model at 0.5 m resolution were released in June 2020 and are currently available at the website in Data and Resources. In addition to this airborne lidar product, both low-altitude airborne imagery and ground-based mobile and terrestrial lidar surveys have been acquired or planned in localized areas within the NAWSCL.

We expect that the high resolution of the NCALM survey, the ground-based lidar, and low-altitude airborne imagery will allow for the detection of additional fault rupture and ground deformation. These sources may image areas of known fault rupture in much better detail locally than what is included in the provisional maps. In addition, the NCALM survey should provide a very high-quality base map for use in adjusting field and other imagery-based linework to a single spatial reference, thus resolving boundary mismatches and location variations inherent in the provisional maps and observations.

Rupture and ground deformation map data products. Rupture map products are included in the same online USGS data release (Ponti *et al.*, 2020) that holds the site-observation data. Anticipated product releases are as follows:

1. Provisional rupture map with data collected through December 2019 (Fig. 8).
2. Additional provisional rupture maps resulting from new field work and low-altitude imagery products, as new fault traces are identified or when existing traces are better defined.
3. A finalized rupture map that may include updated linework interpreted from NCALM imagery and lidar, where appropriate, and field-based linework adjusted to the NCALM base.

Each product release consists of the following data items as applicable:

1. Rupture linework in shapefile and kmz format, with each line segment fully attributed.
2. Any imagery products used for the rupture map release (e.g., orthorectified low-altitude aerial photography, pixel correlation images, lidar hillshades, etc.) that are not published elsewhere, in GeoTIFF format.

Full documentation is provided in metadata files (FGDC format) for each data item.

Initial Observations

Site-specific field observations, field mapping, and interpretations of surface fault rupture and ground deformation from optical and geodetic image products show that the M_w 6.4 event produced nearly continuous left-lateral surface rupture, with little vertical displacement, for a distance of approximately 18 km (Fig. 1). Approximately 12.5 km of the rupture occurs southwest of the intersection with the M_w 7.1 surface rupture trace. Sinistral slip of more than 1.8 m has been measured along this portion of the rupture, which is observed to splay into several subparallel fault traces to the southwest. Near the rupture's southwestern terminus, the dominant northeast-trending fault strands are crossed by multiple right-lateral, left-stepping en echelon, northwest-striking subsidiary faults. About 3 km to the northeast of the intersection with the M_w 7.1 rupture, the M_w 6.4 rupture steps about 1.4 km to the northwest and continues to the northeast for an additional 2 km, terminating near the M_w 6.4 epicentral location. Two approximately parallel northeast–southwest-trending zones of discontinuous surface faulting and small displacements—one approximately 7 km long zone and located about 3 km to the northwest of the principal M_w 6.4 rupture, and the second located approximately 4 km to the southeast of the principal M_w 6.4 rupture that extends for a length of more than 15 km (Fig. 1)—were likely produced by the M_w 6.4 event, based on interpretations from remote-sensing data that identify deformation near some of the mapped ruptures (Milliner and Donnellan, 2020). However, these features were not documented on the ground until after the larger M_w 7.1 earthquake occurred, and evidence does exist at the intersections with the M_w 7.1 rupture to suggest some local reactivation may have occurred during the M_w 7.1 earthquake. Therefore, the causative earthquake remains somewhat uncertain.

The M_w 7.1 earthquake produced rupture over a length of approximately 50 km, of which more than 35 km is composed

of continuous or nearly continuous rupture along a northwest–southeast strike. Surface faulting is dominated by dextral slip, complicated locally by zones of distributed slip several kilometers wide that consist of two or more subparallel fault traces, or by dextral, sinistral, and normal displacements along short and disconnected, northwest- to northeast-striking fault traces. Both the northwest and southeast rupture terminations are dominated by sinistral northeast–southwest-striking ruptures that step-left along a northwest–southeast trend similar to the strike of the continuous main rupture zone; this pattern is especially prevalent at the northern end of the rupture in which discontinuous zones of northeast and north-striking fault traces extend to the northwest for about 12 km. Numerous observations of peak dextral slip of 4–5+ m are observed near the epicenter, whereas 3–4 m slip extends to the northwest and southeast over a distance of approximately 10 km. Vertical separations are variable, but mostly less than 1 m and dominantly down to the west. Peak vertical separation is greatest northwest of the epicenter, in which northeast- and southwest-facing normal to dextral–oblique fault scarps bound an approximately 2 km wide basin (DuRoss *et al.*, 2020).

In addition to surface faulting, the M_w 6.4 and 7.1 events also produced significant liquefaction-related deformation locally, in particular along the west margin of Searles Valley and within and adjacent to playas in the NAWSCL. Slope failures were not extensive, but observations of slope failures and rockfalls on steep slopes and roadcuts were noted in upland areas, particularly near the M_w 6.4 epicenter.

Summary

Postearthquake field investigations focused on the geologic effects of the Ridgecrest earthquake sequence involved more than six dozen scientists from 20 different government, academic, and private institutions. More than 6000 ground observations have been acquired as of December 2019, of which about 4500 include detailed descriptions or photo documentation, with more than 1100 of these also containing quantitative field measurements of fault displacement sense and magnitude. Fault ruptures and ground-deformation features were mapped locally in the field and interpreted from aerial and satellite optical imagery and geodetic image products. These observations and maps are anticipated to be disseminated as a series of digital data products in an online USGS data release (Ponti *et al.*, 2020), initially in provisional form.

Advancements in digital collection of field data, together with the extensive amount of fault rupture and ground deformation produced by the Ridgecrest earthquake sequence, have resulted in a significant volume of data that are available for analysis. Challenges to managing, compiling, disseminating, and interpreting such a large dataset highlight the need to further improve data collection, dissemination, and compilation processes, and for researchers to work toward better standardization of displacement measurements and reporting formats. In addition, more detailed and consistent reporting of observation metadata, specifically the types of equipment and software used for data collection and location determination, and the documentation of uncertainty estimates for quantitative measurements, will not only simplify data compilation, but also improve the ability to assess data quality for interpretive purposes. Such improvements have occurred since the South Napa earthquake of 2014 served as a test bed for applying new technology to improve postearthquake field response. These new data describing the Ridgecrest earthquake sequence provide a rich foundation for future research on earthquake hazards within the eastern California shear zone.

Data and Resources

Provisional datasets are available in a U.S. Geological Survey (USGS) data release product (Ponti *et al.*, 2020; doi: 10.5066/P9BZ5IJ9); this is also the site for anticipated future releases. The data release is structured as a series of pages and child items, with each data product having its own page within the overall data release package. Initially released products include site observations for locations where quantitative fault slip and separation data were collected, and a provisional rupture and ground-deformation map of verified fault traces as of December 2019. The data release is anticipated to be updated as more information is compiled and reviewed. Information on the Earthquake Engineering Research Institute's Virtual Clearinghouse website is available at http://learningfromearthquakes.org/2019-07-04-searles-valley/ and information about Southern California Earthquake Center's (SCEC) earthquake response blog is available at response.scec.org. Data about National Aeronautics and Space Administration's (NASA's) Advanced Rapid Imaging and Analysis (ARIA) data portal are available at https://aria-share.jpl.nasa.gov/ and the USGS Hazards Data Distribution System (HDDS) is available at https://www.usgs.gov/land-resources/hdds/hazards-data-distribution-system-hdds/. The NCALM 2019 Ridgecrest, CA post-earthquake lidar collection is available at doi: 10.5069/G9W0942Z. All websites were last accessed in January 2020.

Acknowledgments

The compilation of fault rupture and ground-deformation observations described herein is only possible because of the direct efforts of researchers from numerous federal and state agencies, universities, and commercial institutions, who participated in fieldwork, scientific coordination, data analysis, and compilation; these researchers are listed as coauthors of this article. The authors wish to thank Misty Ellingson and Andria Bullock, with support of Matthew Boggs and Ole Hendon of the Naval Air Warfare Center Weapons Division, who provided us with airspace access within the Naval Air Weapons Station China Lake (NAWSCL). Mayor Peggy Breeden and Chief of Police Jed McGlaughlin of the City of Ridgecrest welcomed the field teams while they worked in their city. Margo Allen, Helen Haase, Jeff Mayberry, and Rob Gallagher, of the NAWSCL Public affairs Office, provided Operations Security review support, as did John Foster and his entire Unexploded Ordinance team. Angela Roush and the "Joshua'" airspace controllers are also greatly thanked, as are California Highway Patrol (CHP) and

National Guard for helicopter support for field work and planning. The authors also wish to thank Aron Meltzner, Suzanne Hecker, Brian Sherrod, Allison Bent, and an anonymous reviewer for their thorough and thoughtful reviews; their comments have greatly improved the article. This work is principally funded by the National Earthquake Hazards Reduction Program. Portions of this research were carried out at the Jet Propulsion Laboratory, Pasadena, California, U.S.A., under a contract with the National Aeronautics and Space Administration (80NM0018D0004). Any use of trade, product, or firm names is for descriptive purposes only and does not imply endorsement by the U.S. Government.

References

Bennett, S. E. K., T. C. Ladinsky, B. Swanson, A. E. Morelan III, C. W. D. Milliner, K. M. Scharer, R. D. Gold, S. O. Akciz, and T. E. Dawson (2019). Rupture of pre-existing conjugate faults during the M 7.1 earthquake near Ridgecrest, CA, *AGU Fall Meeting 2019 Abstracts*, available at https://agu.confex.com/agu/fm19/meetingapp.cgi/Paper/622719 (last accessed January 2020).

Bilham, R., and B. A. Costello (2019). Creepmeter measurements of triggered slip and afterslip associated with the 2019 Ridgecrest sequence, *AGU Fall Meeting 2019 Abstracts*, available at https://agu.confex.com/agu/fm19/meetingapp.cgi/Paper/619071 (last accessed January 2020).

Dawson, T. E., J. Thompson Jobe, G. Seitz, and M. DeFrisco (2019). Assessing the distribution of mapped faults and surface ruptures related to the 2019 Ridgecrest earthquake sequence: what we knew and what we could have known, *AGU Fall Meeting 2019 Abstracts*, available at https://agu.confex.com/agu/fm19/meetingapp.cgi/Paper/592996 (last accessed January 2020).

Donnellan, A., G. Lyzenga, J. Wang, M. Pierce, and C. Goulet (2019). High-resolution targeted 3D imaging postseismic products of the Ridgecrest M6.4 and M7.1 earthquake sequence, doi: 10.5967/5sq2-rs60.

DuRoss, C. B., R. D. Gold, T. E. Dawson, K. M. Scharer, K. J. Kendrick, S. O. Akciz, S. J. Angster, J. Bachhuber, S. Bacon, S. E. K. Bennett, *et al.* (2020). Surface displacement distributions for the July 2019 Ridgecrest, California, earthquake ruptures, *Bull. Seismol. Soc. Am.*, doi: 10.1785/0120200058.

Earthquake Engineering Research Institute (EERI) (2020). *EERI Earthquake Reconnaissance Summary Report: 2019 Ridgecrest Earthquake Sequence*, Earthquake Engineering Research Institute, Oakland, California.

Gold, R. D., W. D. Barnhart, C. B. DuRoss, T. E. Dawson, K. J. Kendrick, K. M. Scharer, A. E. Morelan, and C. W. D. Milliner (2019). Surface rupture associated with the 2019 Ridgecrest earthquake sequence: Comparison of field-based and remotely sensed observations, *AGU Fall Meeting 2019 Abstracts*, available at https://agu.confex.com/agu/fm19/meetingapp.cgi/Paper/546719 (last accessed January 2020).

Haddon, E. K., S. E. K. Bennett, J. R. Patton, K. J. Kendrick, B. Olson, C. B DuRoss, and A. Pickering (2019). Near-surface fault slip data for the M_w 7.1 Ridgecrest earthquake from curved coseismic striations, *AGU Fall Meeting 2019 Abstracts*, available at https://agu.confex.com/agu/fm19/meetingapp.cgi/Paper/617785 (last accessed January 2020).

Hernandez, J. L., and T. E. Dawson (2019). Triggered slip on the Little Lake Fault Zone resulting from the 2019 Ridgecrest earthquake sequence, California, *AGU Fall Meeting 2019 Abstracts*, available at https://agu.confex.com/agu/fm19/meetingapp.cgi/Paper/621035 (last accessed January 2020).

Hough, S. E., E. Thompson, A. Baltay, G. A. Parker, K. W. Hudnut, R. W. Graves, M. Page, E. S Cochran, K. R. Blake, T E. Dawson, *et al.* (2019). Near-field ground motions from the 2019 M6.4 and M7.1 Ridgecrest, California, earthquakes: Subdued shaking due to pervasive non-linear site response? *AGU Fall Meeting 2019 Abstracts*, available at https://agu.confex.com/agu/fm19/meetingapp.cgi/Paper/558701 (last accessed January 2020).

Hudnut, K. W., J. L. Hernandez, L. Seeber, and J. F. Pacheco (2019). Cross-fault interaction in the July 2019 Ridgecrest earthquake sequence, southern California, *AGU Fall Meeting 2019 Abstracts*, available at https://agu.confex.com/agu/fm19/meetingapp.cgi/Paper/510585 (last accessed January 2020).

Hudnut, K. W., B. A. Brooks, K. Scharer, J. L. Hernandez, T. E. Dawson, M. E. Oskin, J. Ramon Arrowsmith, C. A. Goulet, K. Blake, M. L. Boggs, *et al.* (2020). Airborne lidar and electro-optical imagery along surface ruptures of the 2019 Ridgecrest earthquake sequence, southern California, *Seismol. Res. Lett.* doi: 10.1785/0220190338.

Jones, T. W., L. Marzen, and A. Chappelka (2015). Horizontal accuracy assessment of Global Positioning System data from common smartphones, *Pap. Appl. Geogr.* **1,** 59–64, doi: 10.1080/23754931.2015.1009304.

Kendrick, K., S. Akciz, S. Angster, J. Avouac, J. Bachhuber, S. Bennett, K. Blake, S. Bork, B. Brooks, P. Burgess, *et al.* (2019). Geologic observations of surface fault rupture associated with the Ridgecrest M6.4 and M7.1 earthquake sequence by the Ridgecrest Rupture Mapping Group, *SCEC Annual Meeting 2019 Proc.*, Vol. 29, 186, available at https://files.scec.org/s3fs-public/SCEC2019Proceedings.pdf (last accessed January 2020).

Leprince, S., F. Ayoub, Y. Klinger, and J. P. Avouac (2007). Co-registration of optically sensed images and correlation (COSI-Corr): An operational methodology for ground deformation measurements, *IEEE International Geoscience and Remote Sensing Symposium (IGARSS 2007)*, Barcelona, Spain, 23–28 July, doi: 10.1109/IGARSS.2007.4423207.

Lozos, J. C., and R. A. Harris (2020). Dynamic rupture simulations of the *M* 6.4 and *M* 7.1 July 2019 Ridgecrest, California, earthquakes, *Geophys. Res. Lett.* **47,** e2019GL086020, doi: 10.1029/2019GL086020.

Milliner, C., and A. Donnellan (2020). Using Planet Labs satellite imagery to separate the surface deformation between the July 4th M_w 6.4 foreshock and July 5th M_w 7.1 mainshock during the 2019 Ridgecrest earthquake sequence, *Seismol. Res. Lett.* doi: 10.1785/0220190271.

Mosalam, K., V. Abuchar, J. Archbold, C. Arteta, E. Fischer, S. Gunay, M. Hakhamaneshi, W. Hassan, L. Micheli, S. Muin, *et al.* (2019). StEER—M6.4 and M7.1 Ridgecrest, CA earthquakes on July 4–5, 2019, *Preliminary Virtual Reconnaissance Report (PVRR) DesignSafe-CI*, doi: 10.17603/ds2-xqfh-1631.

Olson, B., and Ridgecrest Earthquake Working Group (2019). Slip distribution, slip sense and slip styles along strike of the Ridgecrest

earthquake sequence surface ruptures, GSA Abstract with Programs, ISSN 0016-759, doi: 10.1130/abs/2019AM-342038.

Pickering, A., K. Thomas, D. J. Ponti, C. M. Rosa, J. L. Hernandez, and J. L. Blair (2019). Rapid synthesis of surface rupture mapping and observation data during response to the 2019 Ridgecrest earthquake sequence, CA, *AGU Fall Meeting 2019 Abstracts*, available at https://agu.confex.com/agu/fm19/meetingapp.cgi/Paper/624906 (last accessed January 2020).

Pierce, I., A. Williams, R. D. Koehler, and C. Chupik (2020). High resolution structure-from-motion models and orthophotos of the southern sections of the 2019 M_w 7.1 and M_w 6.4 Ridgecrest earthquakes surface ruptures, *Seismol. Res. Lett.* doi: 10.1785/0220190289.

Pollitz, F. P., J. R. Murray, S. E. Minson, E. Phillips, J. L. Svarc, C. W. Wicks, M. H. Murray, T. L. Ericksen, B. A. Brooks, E. A. Roeloffs, *et al.* (2019). Observations and models of crustal deformation transients following the 2019 Ridgecrest, California, earthquake sequence, *AGU Fall Meeting 2019 Abstracts*, available at https://agu.confex.com/agu/fm19/meetingapp.cgi/Paper/547735 (last accessed January 2020).

Ponti, D. J., C. M. Rosa, and J. L. Blair (2019a). The M_w 6.0 South Napa earthquake of August 24, 2014—Observations of surface faulting and ground deformation, with recommendations for improving post-earthquake field investigations, *U.S. Geol. Surv. Open-File Rept. 2019–1018*, 50 pp., 15 appendixes, doi: 10.3133/ofr20191018.

Ponti, D. J., C. M. Rosa, and J. L. Blair (2019b). Digital datasets documenting fault rupture and ground deformation features produced by the Mw 6.0 South Napa earthquake of August 24, 2014, *U.S. Geol. Surv. Data Release*, doi: 10.5066/F7P26W84.

Ponti, D. J., J. L. Blair, C. M. Rosa, K. Thomas, A. J. Pickering, and T. E. Dawson, compilers (2020). Digital datasets documenting surface fault rupture and ground deformation features produced by the Ridgecrest M6.4 and M7.1 earthquake sequence of July 4 and 5, 2019, *U.S. Geol. Surv. Data Release*, doi: 10.5066/P9BZ5IJ9.

Scharer, K. M., S. O. Akciz, S. E. K. Bennett, T. Dawson, C. B. DuRoss, R. D. Gold, B. Swanson, B. A. Brooks, A. E. Morelan III, C. W. D. Milliner, *et al.* (2019). Fault-normal rupture displacement gradients and the Ridgecrest earthquake sequence of 2019, *AGU Fall Meeting 2019 Abstracts*, available at https://agu.confex.com/agu/fm19/meetingapp.cgi/Paper/548701 (last accessed January 2020).

Stewart, J. P., S. J. Brandenberg, P. Wang, C. C. Nweke, K. Hudson, S. Mazzoni, Y. Bozorgnia, K. W. Hudnut, C. A. Davis, S. K. Ahdi, *et al.* (2019). Preliminary report on engineering and geological effects of the July 2019 Ridgecrest earthquake sequence, *Geotechnical Extreme Events Reconnaissance Association Rept. GEER-064*, doi: 10.18118/G6H66K.

Thomas, A., D. Goldberg, D. Melgar, V. Sahakian, B. Crowell, and J. Geng (2019). The complex kinematics and multi-fault rupture process of the 2019 Ridgecrest earthquakes, *AGU Fall Meeting 2019 Abstracts*, available at https://agu.confex.com/agu/fm19/meetingapp.cgi/Paper/600066 (last accessed January 2020).

Thompson Jobe, J. A., T. E. Dawson, R. D. Gold, C. B. DuRoss, and G. Seitz (2019). Geomorphic evidence of late Quaternary faulting along the M7.1 Ridgecrest earthquake rupture, *AGU Fall Meeting 2019 Abstracts*, available at https://agu.confex.com/agu/fm19/meetingapp.cgi/Paper/611033 (last accessed January 2020).

U.S. Geological Survey and California Geological Survey (USGS and CGS) (2006). Quaternary fault and fold database of the United States: U.S. Geological Survey database, available at https://earthquake.usgs.gov/hazards/qfaults/ (last accessed August 2019).

Authors and Affiliations

Daniel J. Ponti: U.S. Geological Survey, Moffett Field, California, U.S.A.; **James Luke Blair:** U.S. Geological Survey, Moffett Field, California, U.S.A.; **Carla M. Rosa:** California Department of Conservation, California Geological Survey, San Mateo, California, U.S.A.; **Kate Thomas:** California Department of Conservation, California Geological Survey, Sacramento, California, U.S.A.; **Alexandra J. Pickering:** U.S. Geological Survey, Moffett Field, California, U.S.A.; **Sinan Akciz:** Department of Geological Sciences, California State University, Fullerton, Fullerton, California, U.S.A.; **Stephen Angster:** U.S. Geological Survey at Department of Earth and Space Sciences, University of Washington, Seattle, Washington, U.S.A.; **Jean-Philipe Avouac:** Division of Geological and Planetary Sciences, Pasadena, California, U.S.A., Pasadena, California, U.S.A.; **Jeffrey Bachhuber:** Geosciences Department, Pacific Gas & Electric Company, San Francisco, California, U.S.A.; **Steven Bacon:** Naval Earth Sciences and Engineering Program, Desert Research Institute, Reno, Nevada, U.S.A.; **Nicolas Barth:** Earth and Planetary Sciences Department, University of California, Riverside, Riverside, California, U.S.A.; **Scott Bennett:** U.S. Geological Survey, Moffett Field, California, U.S.A.; **Kelly Blake:** Naval Air Weapons Station, China Lake, Ridgecrest, California, U.S.A.; **Stephan Bork:** Naval Air Weapons Station, China Lake, Ridgecrest, California, U.S.A.; **Benjamin Brooks:** U.S. Geological Survey, Moffett Field, California, U.S.A.; **Thomas Bullard:** Naval Earth Sciences and Engineering Program, Desert Research Institute, Reno, Nevada, U.S.A.; **Paul Burgess:** California Department of Conservation, California Geological Survey, Sacramento, California, U.S.A.; **Colin Chupik:** Mackay School of Earth Sciences and Engineering, University of Nevada, Reno, Nevada, U.S.A. Now at Bureau of Reclamation, Denver, Colorado, U.S.A.; **Timothy Dawson:** California Department of Conservation, California Geological Survey, San Mateo, California, U.S.A.; **Michael DeFrisco:** California Department of Conservation, California Geological Survey, Los Angeles, California, U.S.A.; **Jaime Delano:** U.S. Geological Survey, Golden, Colorado, U.S.A.; **Stephen DeLong:** U.S. Geological Survey, Moffett Field, California, U.S.A.; **James Dolan:** University of Southern California, Los Angeles, California, U.S.A.; **Andrea Donnellan:** Jet Propulsion Laboratory, Pasadena, California, U.S.A., Pasadena, California, U.S.A.; **Christopher DuRoss:** U.S. Geological Survey, Golden, Colorado, U.S.A.; **Todd Ericksen:** U.S. Geological Survey, Moffett Field, California, U.S.A.; **Erik Frost:** California Department of Conservation, California Geological Survey, Los Angeles, California, U.S.A.; **Gareth Funning:** Earth and Planetary Sciences Department, University of California, Riverside, Riverside, California, U.S.A.; **Ryan Gold:** U.S. Geological Survey, Golden, Colorado, U.S.A.; **Nicholas Graehl:** California Department of Conservation, California Geological Survey, Sacramento, California, U.S.A.; **Carlos Gutierrez:** California Department of Conservation, California Geological Survey,

Sacramento, California, U.S.A.; **Elizabeth Haddon:** U.S. Geological Survey, Moffett Field, California, U.S.A.; **Alexandra Hatem:** University of Southern California, Los Angeles, California, U.S.A. Now at U.S. Geological Survey, Golden, Colorado, U.S.A.; **John Helms:** High Desert Consulting, Inc., Palmdale, California, U.S.A.; **Janis Hernandez:** California Department of Conservation, California Geological Survey, Los Angeles, California, U.S.A.; **Christopher Hitchcock:** InfraTerra, San Francisco, California, U.S.A.; **Peter Holland:** California Department of Conservation, California Geological Survey, Sacramento, California, U.S.A.; **Kenneth Hudnut:** U.S. Geological Survey, Pasadena, California, U.S.A.; **Katherine Kendrick:** U.S. Geological Survey, Pasadena, California, U.S.A.; **Richard Koehler:** Mackay School of Earth Sciences and Engineering, University of Nevada, Reno, Reno, Nevada, U.S.A.; **Ozgur Kozaci:** InfraTerra, San Francisco, California, U.S.A.; **Tyler Ladinsky:** California Department of Conservation, California Geological Survey, San Mateo, California, U.S.A.; **Robert Leeper:** Haley & Aldrich, Costa Mesa, California, U.S.A. Now at Earthquake Answers, Whittier, California, U.S.A.; **Christopher Madugo:** Geosciences Department, Pacific Gas & Electric Company, San Francisco, California, U.S.A.; **Maxime Mareschal:** California Department of Conservation, California Geological Survey, San Mateo, California, U.S.A.; **James McDonald:** Environmental Resources and Assessment (EV4), NAVFAC Northwest, Silverdale, Washington, U.S.A.; **Devin McPhillips:** U.S. Geological Survey, Pasadena, California, U.S.A.; **Christopher Milliner:** Jet Propulsion Laboratory, Pasadena, California, U.S.A., Pasadena, California, U.S.A.**Daniel Mongovin:** U.S. Geological Survey, Moffett Field, California, U.S.A.; **Alexander Morelan:** California Department of Conservation, California Geological Survey, Sacramento, California, U.S.A.; **Stephanie Nale:** Naval Air Weapons Station, China Lake, Ridgecrest, California, U.S.A.; **Johanna Nevitt:** U.S. Geological Survey, Moffett Field, California, U.S.A.; **Matt O'Neal:** California Department of Conservation, California Geological Survey, Sacramento, California, U.S.A.; **Brian Olson:** California Department of Conservation, California Geological Survey, Los Angeles, California, U.S.A.; **Michael Oskin:** Earth and Planetary Sciences Department, University of California, Davis, Davis, California, U.S.A.; **Salena Padilla:** Department of Geological Sciences, California State University, Fullerton, Fullerton, California, U.S.A.; **Jason Patton:** California Department of Conservation, California Geological Survey, Sacramento, California, U.S.A.; **Belle Philibosian:** U.S. Geological Survey, Moffett Field, California, U.S.A.; **Ian Pierce:** Mackay School of Earth Sciences and Engineering, University of Nevada, Reno, Nevada, U.S.A.; **Cynthia Pridmore:** California Department of Conservation, California Geological Survey, Sacramento, California, U.S.A.; **Nathaniel Roth:** California Department of Conservation, California Geological Survey, Sacramento, California, U.S.A.; **David Sandwell:** Scripps Institution of Oceanography, University of California, San Diego, La Jolla, California, U.S.A.; **Katherine Scharer:** U.S. Geological Survey, Pasadena, California, U.S.A.; **Gordon Seitz:** California Department of Conservation, California Geological Survey, San Mateo, California, U.S.A.; **Drake Singleton:** Scripps Institution of Oceanography, University of California, San Diego, La Jolla, California, U.S.A.; **Bridget Smith-Konter:** Department of Earth Sciences, University of Hawaii at Manoa, Honolulu, Hawaii, U.S.A.; **Eleanor Spangler:** California Department of Conservation, California Geological Survey, Sacramento, California, U.S.A.; **Brian Swanson:** California Department of Conservation, California Geological Survey, Los Angeles, California, U.S.A.; **Jessica Thompson Jobe:** U.S. Geological Survey, Golden, Colorado, U.S.A. Now at Bureau of Reclamation, Denver, Colorado, U.S.A.; **Jerome Treiman:** California Department of Conservation, California Geological Survey, Los Angeles, California, U.S.A.; **Francesca Valencia:** California Department of Conservation, California Geological Survey, Los Angeles, California, U.S.A.; **Joshua Vanderwal:** Haley & Aldrich, Costa Mesa, California, U.S.A.; **Alana Williams:** School of Earth and Space Exploration, Arizona State University, Tempe, Arizona, U.S.A.; **Xiaohua Xu:** Scripps Institution of Oceanography, University of California, San Diego, La Jolla, California, U.S.A.; **Judith Zachariasen:** California Department of Conservation, California Geological Survey, Sacramento, California, U.S.A.; **Jade Zimmerman:** NAVFAC-SW, NAWS China Lake, Ridgecrest, California, U.S.A.; and **Robert Zinke:** Jet Propulsion Laboratory, Pasadena, California, U.S.A., Pasadena, California, U.S.A.

Manuscript received 22 October 2019
Published online 29 July 2020